A&A 621, A34 (2019)
https://doi.org/10.1051/0004-6361/201833879

Astronomy & Astrophysics

Deriving the Hubble constant using *Planck* and *XMM-Newton* observations of galaxy clusters

Arpine Kozmanyan[1,2], Hervé Bourdin[1,2], Pasquale Mazzotta[1,2], Elena Rasia[3], and Mauro Sereno[4,5]

[1] Dipartimento di Fisica,Università di Roma "Tor Vergata", Via della Ricerca Scientifica 1, 00133 Roma, Italy
e-mail: arpine.kozmanyan@roma2.infn.it
[2] Sezione INFN Roma 2, Via della Ricerca Scientifica 1, 00133 Roma, Italy
[3] INAF, Osservatorio Astronomico di Trieste, Via Tiepolo 11, 34131 Trieste, Italy
[4] INAF – Osservatorio di Astrofisica e Scienza dello Spazio di Bologna, Via Piero Gobetti 93/3, 40129 Bologna, Italy
[5] Dipartimento di Fisica e Astronomia, Alma Mater – Universita di Bologna, Via Piero Gobetti 93/2, 40129 Bologna, Italy

Received 16 July 2018 / Accepted 25 September 2018

ABSTRACT

The possibility of determining the value of the Hubble constant using observations of galaxy clusters in X-ray and microwave wavelengths through the Sunyaev Zel'dovich (SZ) effect has long been known. Previous measurements have been plagued by relatively large errors in the observational data and severe biases induced, for example, by cluster triaxiality and clumpiness. The advent of *Planck* allows us to map the Compton parameter y, that is, the amplitude of the SZ effect, with unprecedented accuracy at intermediate cluster-centric radii, which in turn allows performing a detailed spatially resolved comparison with X-ray measurements. Given such higher quality observational data, we developed a Bayesian approach that combines informed priors on the physics of the intracluster medium obtained from hydrodynamical simulations of massive clusters with measurement uncertainties. We applied our method to a sample of 61 galaxy clusters with redshifts up to $z < 0.5$ observed with *Planck* and *XMM-Newton* and find $H_0 = 67 \pm 3\,\mathrm{km\,s^{-1}\,Mpc^{-1}}$.

Key words. cosmological parameters – distance scale – galaxies: clusters: intracluster medium – X-rays: galaxies: clusters – galaxies: clusters: general

1. Introduction

The X-ray radiation from galaxy clusters and the spectral distortion of the cosmic microwave background (CMB) radiation by inverse Compton scattering of CMB photons (Sunyaev-Zel'dovich effect, SZ) are both due to the electrons in the intracluster medium (ICM; Sarazin 2009; Sunyaev & Zeldovich 1970). The amplitudes of the two effects have different dependence on the density of the electrons in the ICM. The two effects can be jointly used to break the degeneracy existing in the amplitudes of the signals between the cluster electron density and the angular diameter distance to the cluster. Some early works by Cowie & Perrenod (1978), Gunn et al. (1979), Silk & White (1978) and Cavaliere et al. (1979) proposed this method to constrain cosmological parameters such as the Hubble constant, the deceleration parameter, or the flatness of the universe. A well-known advantage of the method is that it does not depend on any secondary cosmic scales and is based on very simple principles.

Early estimations by Birkinshaw (1979), Reese et al. (2000, 2002), Patel et al. (2000), Mason et al. (2001), Sereno (2003), Udomprasert et al. (2004), Schmidt et al. (2004) and Jones et al. (2005) and others relied on data from ground-based low-frequency (10–150 GHz) radio interferometers detecting the decrement side of the thermal SZ (tSZ) distortion. As an example, Reese et al. (2004) combined SZ measurements from the Ryle telescope (RT), Owens Valley Radio Observatory (OVRO) and the Berkeley-Illinois-Maryland Association (BIMA) observatories and X-ray measurements from the ROSAT satellite for 26 clusters within redshift $z \leq 0.78$ and found a value of $H_0 = 61 \pm 3(\mathrm{stat.}) \pm 18(\mathrm{sys.})\,\mathrm{km\,s^{-1}\,Mpc^{-1}}$ for a flat Λ cold dark matter (CDM) cosmology with $\Omega_\mathrm{m} = 0.3$ and $\Omega_\Lambda = 0.7$. Using SZ measurements from the OVRO, BIMA, and X-ray measurements from the *Chandra* observatory for 38 clusters in the redshift range $0.14 \leq z \leq 0.89$, Bonamente et al. (2006) estimated $H_0 = 76.9^{+3.9}_{-3.4}(\mathrm{stat.})^{+10.0}_{-8.0}(\mathrm{sys.})\,\mathrm{km\,s^{-1}\,Mpc^{-1}}$ for the same cosmological model. A slightly higher accuracy was achieved by Schmidt et al. (2004), who used only three regular clusters at redshifts equal to 0.088, 0.2523, and 0.451 and found $H_0 = 68 \pm 8$, again for the same cosmological model. The authors claimed that they were able to achieve an improved accuracy using only regular systems as the systematic errors are negligible with respect to the statistical ones.

Recent estimates of the Hubble constant from CMB anisotropies by *Planck* Collaboration, ($H_0 = 66.93 \pm 0.62\,\mathrm{km\,s^{-1}\,Mpc^{-1}}$, Planck Collaboration Int. XLVI 2016) have reached a precision that is hard to compete with. Nevertheless, because of the known discrepancy of this value with the value derived by Riess et al. (2018a) using Cepheid-calibrated type Ia supernovae (SNIa) ($H_0 = 73.48 \pm 1.66\,\mathrm{km\,s^{-1}\,Mpc^{-1}}$ or $H_0 = 73.52 \pm 1.62\,\mathrm{km\,s^{-1}\,Mpc^{-1}}$ from Riess et al. 2018b), it is key to have external and independent confirmations. The development of alternative methods will allow us to advance our understanding of the issue and of the potential sources of discrepancy, be they of cosmological or of systematic origin. For this reason, a number of new and promising approaches are brought forward, such as the use of water masers (Reid et al. 2013; Gao et al. 2016), or lensed multiple images of quasars

(Sereno & Paraficz 2014; Wong et al. 2017; Bonvin et al. 2017) or SNe (Grillo et al. 2018).

In line with this thought, and in view of newly available data from the *Planck* space satellite, we revisit the method of determining H_0 using observations of galaxy clusters. The frequency coverage of the CMB spectrum offered by the high-frequency instrument of *Planck* (100–857 GHz) allows mapping the Compton parameter y, that is, the amplitude of the SZ effect, with an unprecedented accuracy at intermediate cluster-centric radii (Bourdin et al. 2017). It thus permits us to perform precise, spatially resolved comparisons with X-ray measurements. Given these measurement accuracies, the limiting factor of the method now becomes our knowledge of the ICM physics and geometry, which motivates the introduction of priors from hydrodynamical simulations of massive clusters. We developed a Bayesian approach that combines such priors with measurement uncertainties. In this paper we discuss this method and its application to a sample of 61 moderately distant galaxy clusters observed with *Planck* and *XMM-Newton*. The method might also allow a future determination of the helium abundance in cluster gas.

The paper is structured as follows. In Sects. 2 and 3 we present the observed and simulated samples, respectively. In Sect. 4 we describe our method. We present the collective characterisation of the most prominent bias sources by making use of simulated galaxy clusters. We applied this information to correct real observations in order to place constraints on cosmological parameters. In Sect. 5 we present our results, and in Sect. 6 we compare them with previous measurements and predict precisions that will be possible using this method.

2. Observed sample

Our sample is derived from the PSZ2 catalogue of SZ-selected clusters by the *Planck* mission. The set of clusters used for this work is almost identical to the set used in Planck Collaboration XI (2011) for the X-ray – SZ scaling relations. The original set counted 62 clusters in total, but one of them (*ZwCl*1215 + 0400) was later excluded from the second *Planck* catalogue of SZ sources. In this work, we removed this cluster and used a total of 61 galaxy clusters in the redshift range $0 < z < 0.5$. The mass range of the clusters in the sample is $2.6 \times 10^{14}\,M_\odot \leq M_{500} \leq 1.8 \times 10^{15}\,M_\odot$.

Studies of cluster populations selected in SZ and X-ray surveys indicate that SZ-selected samples could be a fair representation of the general population of clusters in the universe (Rossetti et al. 2016, 2017; Sereno et al. 2017; Andrade-Santos et al. 2017). Unlike flux-limited X-ray selected cluster populations that seem to preferentially include dynamically relaxed and cool-core clusters, the SZ-selected clusters do not exhibit such preference (Rossetti et al. 2016, 2017; Andrade-Santos et al. 2017). The clusters selected via SZ appear to be unbiased representatives of the overall cluster population since their density profile and concentrations are consistent with standard predictions of ΛCDM cosmology (Sereno et al. 2017).

As described in Planck Collaboration XI (2011), because the selection of our sample combines both SZ and X-ray criteria, we cannot fully claim that the dataset used in our analysis is representative or complete. It represents a large sample of clusters observed homogeneously with multi-frequency milimetric and X-ray observations of suitable angular resolution, however, allowing us to keep the statistical errors to the minimum. In the near future, large cluster projects within the Heritage program[1] of *XMM-Newton* will resolve this specific issue and provide access to large samples of mass-selected clusters.

3. Simulated sample

We used the hydrodynamical simulations of galaxy clusters presented in Rasia et al. (2015). They were carried out with the improved version of the TreePM-smooth-particle-hydrodynamics code GADGET-3 (Springel 2005) introduced in Beck et al. (2016). The runs considered uniform time-dependent ultraviolet (UV) background and a radiative cooling that is metallicity dependent (Wiersma et al. 2009). Star formation and evolution were modelled in a sub-resolution fashion from a multi-phase gas as in Springel & Hernquist (2003). Metals were produced by SNIa, SNII, and asymptotic-giant-branch stars as in Tornatore et al. (2007). Galactic winds of velocity $350\,\mathrm{km\,s^{-1}}$ mimicked the kinetic feedback by SN. The active galactic nucleus (AGN) feedback followed the Steinborn et al. (2015) model, where both mechanical outflows and radiation were evaluated separately. Their combined effect was implemented in terms of thermal energy. Only cold accretion onto the black holes was considered, which was computed by multiplying the Bondi rate by a boost factor $\alpha = 100$. The accretion was Eddington limited. Further details can be found in Rasia et al. (2015), Planelles et al. (2017) and Biffi et al. (2017).

The cosmological model in the simulation assumes a flat ΛCDM cosmology with $H_0 = 72\,\mathrm{km\,s^{-1}\,Mpc^{-1}}$ and $\Omega_\mathrm{m} = 0.24$ and a fraction of hydrogen mass $X = 0.76$.

These simulations agree largely in their properties with those exhibited by samples of observed clusters. For instance, a comparison of their entropy profiles with the profiles measured by Pratt et al. (2007) shows a remarkable agreement (Rasia et al. 2015). The pressure profiles from Planelles et al. (2017) are in line with the observational results by Arnaud et al. (2010), Planck Collaboration V (2013), Sayers et al. (2013), Sun et al. (2011) and Bourdin et al. (2017). They find general agreement between simulated and observed sets within $0.2 \leq r/R_{500} \leq 1$. They also study the properties of the clumpiness of this set and show that the 3D median radial distribution of the clumping factor at $z = 0$ is in reasonable agreement with observations by Eckert et al. (2015) – the largest observational sample studied for clumpiness so far. Finally, Biffi et al. (2017) compared radial profiles of iron abundance with the observations of Leccardi & Molendi (2008) and found agreement within the dispersion of the simulated profiles.

We here analyse clusters with masses in the range $2.6 \times 10^{14}\,M_\odot \leq M_{500} \leq 1.8 \times 10^{15}\,M_\odot$ at different redshifts. Namely, (i) 26 galaxy clusters at $z = 0$, (ii) 25 clusters at $z = 0.25$, and (iii) 21 clusters at $z = 0.5$. This subsample was chosen from the overall sample of Rasia et al. (2015) to ensure similar mass ranges for the observed and simulated clusters. In Fig. 1 we show the mass distributions of the two samples. The two distributions have similar shape and medians: $7.3 \times 10^{14}\,M_\odot$ and $7.8 \times 10^{14}\,M_\odot$ for the observed and simulated sets, respectively. This also demonstrates that the balance of low- and high-mass clusters in the two sets is comparable.

In order to increase the sample size, we took three perpendicular projections of each cluster and calculated them as three different clusters. This gave us a total sample size of 216 clusters. It is important to note that the different projections and redshift

[1] E.g. witnessing the culmination of structure formation in the universe galaxies, groups of galaxies, clusters of galaxies, and superclusters, PI M. Arnaud and S. Ettori.

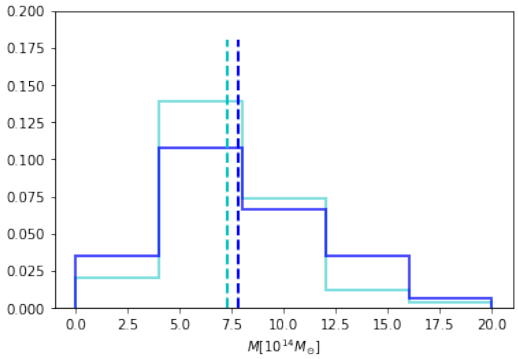

Fig. 1. Normalised mass distributions of observed and simulated samples. In cyan we plot the mass distribution in the observed sample. The dashed line represents the median of the distribution at $7.3 \times 10^{14}\ M_\odot$. In blue we show the mass distribution in the simulated set. The dashed line represents the median at $7.8 \times 10^{14}\ M_\odot$.

snapshots of the same clusters are not completely independent. In Appendix B we present arguments that ensure that the overall distribution created in this way does not introduce additional biases due to correlation between the sample constituents.

The redshift ranges and mass distribution of the simulated sample are thus similar to those of the observed sample. This and the above-mentioned proximity of the simulated cluster properties to the properties of observed clusters indicates that the simulated clusters provide a fair representation of the observed set of clusters used in this analysis.

4. Method

In this section we describe the procedure we followed to estimate the value of H_0 using SZ and X-ray observations. This can be subdivided into three stages: i) joint deprojection of the ICM profiles given the SZ and X-ray observables, ii) characterisation of biases of non-cosmological origin, and iii) estimating the value of the Hubble constant.

4.1. Joint deprojection of the ICM profiles

To estimate the 3D electron number density n_e, temperature kT, and pressure P_e profiles, we used the fitting procedure of Bourdin et al. (2017), which we summarise below.

4.1.1. Derivation of $n_e(r)$

First, X-ray data were used to constrain the 3D $n_e(r)$ profile and to provide an initial approximation of the $kT(r)$ profile. We assumed spherical symmetry and modelled the observable quantities with the analytical profiles suggested by Vikhlinin et al. (2006). More specifically, for the electron number density, we used

$$n_p n_e(r) = \frac{n_0^2 (r/r_c)^{-\alpha'}}{[1+(r/r_c)^2]^{3\beta_1-\alpha'/2}} \frac{1}{[1+(r/r_s)^\gamma]^{\epsilon/\gamma}} + \frac{n_{02}^2}{[1+(r/r_{c2})^2]^{3\beta_2}}, \quad (1)$$

where r_c and r_{c2} are the characteristic radii of β-like profiles with slopes β_1 and β_2, with a power-law cusp modification parametrised with the index α'; n_0 and n_{02} are the normalisations of the two components at the centre; and r_s is the characteristic radius in the outer steeper regions of the profile with slope ϵ.

For the temperature we used

$$kT(r) = T_0 \frac{x + T_{min}/T_0}{x+1} \frac{(r/r_t)^{-a}}{(1+(r/r_t)^b)^{c/b}}, \quad (2)$$

where $x \equiv (r/r_{cool})^{a_{cool}}$, and r_{cool} describes the scale of the central cooling region with slope a_{cool} and normalisation T_{min}; r_t, a, b, and c describe the size and profile slopes outside the cooling region; and T_0 is the overall normalisation of the profile.

After integrating these 3D models along the line of sight (LOS),

$$\Sigma_x(r) = \frac{1}{4\pi(1+z)^3} \int [n_p n_e](r)\Lambda(T,Z)\mathrm{d}l, \quad (3)$$

$$kT_X(r) = \frac{\int wkT(r)\mathrm{d}l}{\int w\mathrm{d}l}, \text{ with } w = n_e^2/T^{3/4}, \quad (4)$$

we fit them jointly to the observed projected X-ray surface brightness $\Sigma_x^{obs}(r)$ and temperature $kT_X^{obs}(r)$ profiles obtained from *XMM-Newton* (see Bourdin et al. 2017 for details).

In Eq. (3) the surface brightness has units cnt s^{-1} cm^{-2} arcmin^{-2}. If energy units are used, such as erg s^{-1} cm^{-2} arcmin^{-2}, then the factor $1+z$ in the denominator would be to the fourth power, that is, $\Sigma_x(r) = \frac{1}{4\pi(1+z)^4} \int [n_p n_e](r)\Lambda(T,Z)\mathrm{d}l$. In Eq. (4) the temperature weighting from Mazzotta et al. (2004) is used.

Modelling the factor $\Lambda(T,Z)$ assumes dependence on the metallicity of the gas and weak dependence on temperature. The first was modelled assuming a redshifted, Galactic-hydrogen-absorbed spectral energy distribution (SED) of hot gas with bremsstrahlung continuum and metal emission lines as tabulated in the Astrophysical Plasma Emission Code (APEC, Smith et al. 2001). We adopted the solar composition of metal abundances tabulated by Grevesse & Sauval (1998) and a constant normalisation of 0.3. The fit of the $kT(r)$ in this part of the procedure took care of the weak temperature dependence of the factor $\Lambda(T,Z)$.

Finally, we derived the electron number density profile $n_e(r) = \sqrt{n_e/n_p \times [n_p n_e](r)}$ assuming $n_p/n_e = 0.852$, which corresponds to a helium abundance of $Y = 0.2527$ for the metal abundances cited above.

4.1.2. Derivation of $P(r)$ and $kT(r)$

In the second step, we jointly fit the X-ray projected temperature $kT_X^{obs}(r)$ and SZ $y^{obs}(r)$ signal profiles. $kT_X^{obs}(r)$ was extracted from the *XMM-Newton*, while $y^{obs}(r)$ was extracted from the six *Planck* HFI maps (see Bourdin et al. 2017 for details).

To model the SZ signal, we used the analytical gNFW pressure profile from Nagai et al. (2007):

$$P_e(r) = \frac{P_0}{(c_{500}x)^\gamma (1+(c_{500}x)^\alpha)^{(\beta-\gamma)/\alpha}}, \quad (5)$$

with $x \equiv r/r_{500}$ and r_{500} being defined as the radius of the cluster within which the mean density of the cluster is 500 times higher than the critical density of the Universe at the clusters redshift. P_0 is the overall normalisation of the profile, c_{500} is the concentration with respect to r_{500}, and α, β, and γ are the slopes at the inner, intermediate, and outer regions of the profile, respectively.

By fixing the $n_e(r)$ profile to the form obtained in the previous step, we created a template for the temperature as

$$kT(r) = \eta_T \times P_e(r)/n_e(r). \quad (6)$$

We then integrated Eqs. (5) and (6) along the LOS using

$$y(r) = \frac{\sigma_T}{m_e c^2} \int P_e(r) \times \mathrm{d}l \tag{7}$$

for the pressure profile and Eq. (4) for the temperature, and we fit them jointly to the observed projected $y^{\rm obs}(r)$ and $T_X^{\rm obs}(r)$ profiles. In addition to estimating the 3D pressure profile $P_e(r)$, this procedure also returns the value of the normalisation parameter η_T, which reflects the discrepancy between the measurement of pressure profile using only X-ray or SZ observables.

In the ideal case of spherical symmetry with no clumpiness, we expect $\eta_T = 1$. In the realistic case, instead, η_T is expected to be different from 1, and its departure depends on different aspects such as the assumptions of the underlying cosmological model and/or some ICM distribution properties (elongation, orientation, clumpiness, etc.).

As shown in Appendix A, η_T has a simple dependence from the main properties that can be divided into two terms:

$$\eta_T = C \times \mathcal{B}. \tag{8}$$

The first term depends only on quantities that are directly related to the cosmological parameters (such as H_0, or Y). It is defined as

$$C = \left(\frac{\bar{D}_a}{D_a}\right)^{1/2} \times \left(\frac{n_{\rm p}/n_{\rm e}}{\bar{n}_{\rm p}/\bar{n}_{\rm e}}\right)^{1/2} \times \left(\frac{1 + 4\frac{n_{\rm He}}{n_{\rm p}}}{1 + 4\frac{\bar{n}_{\rm He}}{\bar{n}_{\rm p}}}\right)^{1/2}, \tag{9}$$

where D_a is the angular diameter distance, $n_{\rm p}/n_{\rm e}$ is the ratio of the hydrogen to electron number density, and $\frac{n_{\rm He}}{n_{\rm p}}$ the ratio of helium to hydrogen number density. The latter two factors both depend on the helium abundance Y in the cluster gas (see Appendix A).

The second term contains everything else that is not directly related to the cosmological model or the helium abundance. It can be parametrised as

$$\mathcal{B} = b_n \frac{C_\rho^{1/2}}{e_{\rm LOS}^{1/2}}, \tag{10}$$

where $e_{\rm LOS}$ is a factor that accounts for the cluster asphericity, $C_\rho = \frac{\langle\rho^2\rangle}{\langle\rho\rangle^2}$ accounts for the cluster clumpiness, and the factor b_n denotes any other bias that could arise from our profile modelling and/or the fitting procedure.

In the previous two formulas, the non-bar and bar notations of parameters refer to their true values and to the values assumed in the data analysis above, respectively. More specifically, we used a ΛCDM cosmological model with $\bar{H}_0 = 70\,{\rm km\,s^{-1}\,Mpc^{-1}}$, $\bar{\Omega}_{\rm m} = 0.3$ and $\bar{\Omega}_\Lambda = 0.7$, $\bar{n}_{\rm p}/\bar{n}_{\rm e} = 0.852$, and $\frac{\bar{n}_{\rm He}}{\bar{n}_{\rm p}} = 0.0851$. For a fully ionised medium, the latter correspond to an assumption of a helium abundance of $\bar{Y} = 0.2527$. We refer to Appendix A for a detailed derivation of the Eqs. (8)–(10) above. To constrain the cosmological quantities, we need to characterise the contribution of the $\mathcal{B}$ term, which is addressed in the next subsection.

4.2. Characterisation of $\mathcal{B}$

To characterise the $\mathcal{B}$ term in Eq. (8), we adopted a simple procedure based on the use of our set of cosmological hydrodynamic simulations that have a clumpiness level comparable to that of real clusters Eckert et al. (2015) and Planelles et al. (2017).

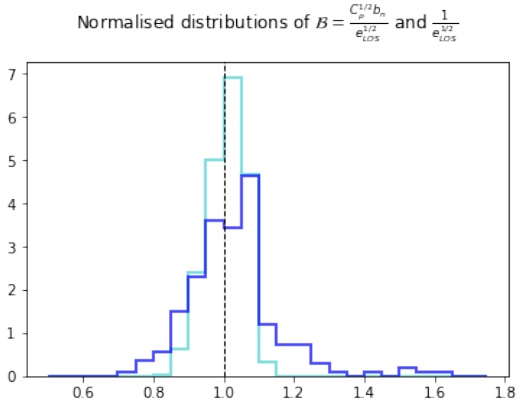

Fig. 2. Distribution of the quantity $\frac{1}{e_{\rm LOS}^{1/2}}$ that was calculated semi-analytically (cyan). Distribution of the quantity $\mathcal{B} \equiv \frac{C_\rho^{1/2}}{e_{\rm LOS}^{1/2}} b_n$, which we used as a prior in our Bayesian estimation of the Hubble constant (blue). The dashed line at value 1 is shown for reference.

We assumed that the cosmological parameters are known, and we fixed them to the values we used for the simulated sample, that is, a flat ΛCDM cosmology with $H_0 = 72\,{\rm km\,s^{-1}\,Mpc^{-1}}$ and $\Omega_{\rm m} = 0.24$, a ratio of hydrogen to electrons $n_{\rm p}/n_{\rm e} = 0.864$, and a number density of helium to hydrogen $n_{\rm He}/n_{\rm p} = 0.0789$ from the fraction of hydrogen mass $X = 0.76$ (see Sect. 3). These assumptions guarantee that for the simulated sample $C = 1$ (see Eq. (9)). Then, for every simulated cluster, we estimated the parameter η_T applying the exact same procedure used for the real clusters.

In this respect, to imitate the "observed" 2D quantities, we projected the simulated cluster properties by integrating along 10 Mpc in the direction of LOS:

$$\Sigma_x(r_{\rm min}, r_{\rm max}) = \frac{\sum m_i \rho_i}{A_{{\rm ring}[r_{\rm min}, r_{\rm max}]}/\pi}, \tag{11}$$

$$T_X(r_{\rm min}, r_{\rm max}) = \frac{\sum T_i w_i V_i}{\sum T_i V_i}, \tag{12}$$

and

$$y(r_{\rm min}, r_{\rm max}) = \frac{\sigma_T}{m_e c^2} \frac{\sum P_i V_i}{A_{{\rm ring}[r_{\rm min}, r_{\rm max}]}}, \tag{13}$$

with the sum extending to all particles within a cylinder of radius $[r_{\rm min}, r_{\rm max}]$ and height 10 Mpc; m_i, ρ_i, T_i, P_i, and V_i being the mass, density, temperature, pressure, and the volume of the ith particle, respectively, w_i is the spectroscopic-like weight equal to $w_i = \rho_i^2/T_i^{3/4}$ (Mazzotta et al. 2004), and $A_{{\rm ring}[r_{\rm min}, r_{\rm max}]} = \pi(r_{\rm max}^2 - r_{\rm min}^2)$ is the surface area of the cylinders base.

In Fig. 2 we show as a blue histogram the η_T distribution resulting from this procedure. Assuming that the simulated clusters accurately approximate the real ones in terms of i) shape, the gas shape at r_{500} does not strongly depend on the ICM physics and mostly follows the total potential of the cluster (see Lau et al. 2011; Kawahara 2010), and ii) clumpiness level (see Planelles et al. 2017 for comparison), the blue histogram gives the intrinsic distribution of the $\mathcal{B}$ term.

We expect that asphericity will play a major role. To distinguish its effect from that of clumpiness, we derived the distribution of $e_{\rm LOS}^{-0.5}$ using the semi-analytical approach of Sereno et al. (2017), which for completeness we also report in Appendix C. The result is overlaid as a cyan histogram in Fig. 2. Comparing the two distributions in Fig. 2, we see that asphericity is indeed

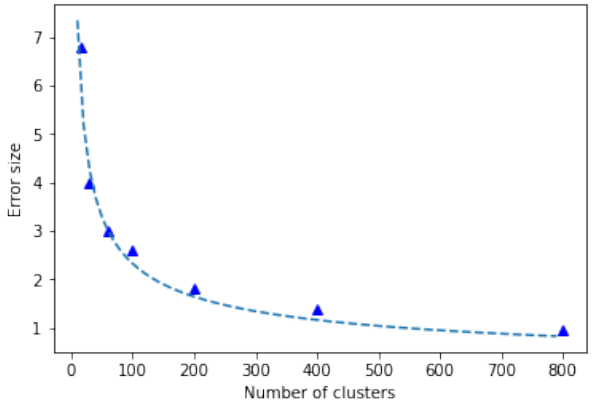

Fig. 6. Prediction of the error depending on the sample size (blue triangles) over-plotted with the function $3.0 \times \left(\frac{60}{N}\right)^{1/2}$ (dashed line).

deuterium abundance). At the same time, BAO in combination with other CMB measurements from the *Wilkinson* Microwave Anisotropy Probe (WMAP), the South-Pole Telescope (SPT), the Atacama Cosmology Telescope (ACT), and SNIa data provide $H_0 = 69.6 \pm 0.7\,\mathrm{km\,s^{-1}\,Mpc^{-1}}$ from Bennett et al. (2014) or in combination with observational Hubble datasets and SNIa data $H_0 = 69.4 \pm 1.7\,\mathrm{km\,s^{-1}\,Mpc^{-1}}$ from Haridasu et al. (2018).

In the light of the possible cosmological solutions suggested so far (Riess et al. 2016; Bernal et al. 2016; Evslin & Sen 2018; Lin & Ishak 2017) that tried to resolve the discrepancy between the CMB and local measurements of H_0, we briefly discuss the importance of these scenarios for our measurement, which is perfectly consistent with the result of Planck Collaboration Int. XLVI (2016) and is compatible within 2σ with Riess et al. (2018a). The current possible cosmological extensions aim to decrease the discrepancy between the CMB measurement and low-redshift SNIa measurements by either modifying early-Universe physics (e.g. BBN, density of relativistic species) in order to increase the CMB result or by changing the late-time evolution of the Universe in order to introduce recent evolution in the value of H_0 allowing for the difference between the early- and late-time measurements. Given that our result is based on low-redshift data, and it is in the lower range of values, modifications of late-time evolution aiming to bring to an increase in the value of H_0 in the local Universe are not required by our findings. The possible modifications in early-time evolution would modify the CMB measurement by moving it towards higher values. In particular, any changes in the value of Y (the only relevant quantity in this work) that were required to reconcile the CMB H_0 constraints with the SNIa would lower our measurement of H_0.

Thus, being a method that does not rely on additional distance ladders, the use of galaxy clusters to determine a local value of the Hubble constant could be decisive in solving this issue in the future. However, more stringent constraints are required for solid conclusions.

6.3. Estimating possible improvements to accuracy

An improvement to the current result could be achieved by applying this method to larger samples. To estimate the accuracy that could be reached, we created a toy model with "measurements" of η_T distributed as our sample (with the same mean and scatter). To these data points we assigned errors equal to the average error on η_T in our data. We then repeated the procedure to fit the value of H_0 for various sizes of our toy sample. In Fig. 6 we report our estimated error size for various sample sizes. We found the final error to vary roughly as the square root of the number of clusters ($\frac{1}{\sqrt{N}}$), as demonstrated in the figure with the overlaid line corresponding to $3.0 \times \left(\frac{60}{N}\right)^{1/2}$. It is remarkable how a future application of this technique to a sample of 200 clusters would narrow down the error on H_0 to a 3% level, as is also shown by the point added to Fig. 5. High-quality *Chandra* and *XMM-Newton* follow-up observations of the *Planck* cluster catalogue are ongoing and are expected provide us with such constraints in the near future.

Acknowledgements. We thank Alex Saro and Balakrishna Sandeep Haridasu for useful discussions, and we acknowledge financial contribution from the agreement ASI-INAF n.2017-14-H.O, from ASI Grant 2016-24-H.0., and from "Tor Vergata" Grant "Mission: Sustainability" EnClOS (E81I18000130005).

References

Abbott, T. M. C., Abdalla, F. B., Annis, J., et al. 2018, MNRAS, 480, 3879
Addison, G. E., Watts, D. J., Bennett, C. L., et al. 2018, ApJ, 853, 119
Ameglio, S., Borgani, S., Diaferio, A., & Dolag, K. 2006, MNRAS, 369, 1459
Andrade-Santos, F., Jones, C., Forman, W. R., et al. 2017, ApJ, 843, 76
Arnaud, M., Pratt, G. W., Piffaretti, R., et al. 2010, A&A, 517, A92
Battaglia, N., Bond, J. R., Pfrommer, C., & Sievers, J. L. 2015, ApJ, 806, 43
Battistelli, E. S., De Petris, M., Lamagna, L., et al. 2003, ApJ, 598, L75
Beck, A. M., Murante, G., Arth, A., et al. 2016, MNRAS, 455, 2110
Bennett, C. L., Larson, D., Weiland, J. L., & Hinshaw, G. 2014, ApJ, 794, 135
Bernal, J. L., Verde, L., & Riess, A. G. 2016, J. Cosmol. Astropart. Phys., 2016, 019
Biffi, V., Planelles, S., Borgani, S., et al. 2017, MNRAS, 468, 531
Birkinshaw, M. 1979, MNRAS, 187, 847
Bonamente, M., Joy, M. K., LaRoque, S. J., et al. 2006, ApJ, 647, 25
Bonamigo, M., Despali, G., Limousin, M., et al. 2015, MNRAS, 449, 3171
Bonvin, V., Courbin, F., Suyu, S. H., et al. 2017, MNRAS, 465, 4914
Bourdin, H., Mazzotta, P., Kozmanyan, A., Jones, C., & Vikhlinin, A. 2017, ApJ, 843, 72
Bryan, G. L., & Norman, M. L. 1998, ApJ, 495, 80
Cavaliere, A., Danese, L., & de Zotti, G. 1979, A&A, 75, 322
Cowie, L. L., & Perrenod, S. C. 1978, ApJ, 219, 354
Eckert, D., Molendi, S., Vazza, F., Ettori, S., & Paltani, S. 2013, A&A, 551, A22
Eckert, D., Roncarelli, M., Ettori, S., et al. 2015, MNRAS, 447, 2198
Evslin, J., Sen, A. A., & Ruchika., 2018, Phys. Rev. D, 97, 103511
Fonnesbeck, C., Patil, A., Huard, D., & Salvatier, J. 2015, Astrophysics Source Code Library [record ascl:1506.005]
Gao, F., Braatz, J. A., Reid, M. J., et al. 2016, ApJ, 817, 128
Grainge, K., Jones, M. E., Pooley, G., et al. 2002, MNRAS, 333, 318
Grevesse, N., & Sauval, A. J. 1998, Space Sci. Rev., 85, 161
Grillo, C., Rosati, P., Suyu, S. H., et al. 2018, ApJ, 860, 94
Gunn, J. E., Longair, M. S., Rees, M. J., & Abell, G. O. 1979, Phys. Today, 32, 58
Haridasu, B. S., Luković, V. V., & Vittorio, N. 2018, J. Cosmol. Astropart. Phys., 2018, 033
Hu, W., & Kravtsov, A. V. 2003, ApJ, 584, 702
Inagaki, Y., Suginohara, T., & Suto, Y. 1995, Publ. Astron. Soc. Jpn., 47, 411
Jones, M. E., Edge, A. C., Grainge, K., et al. 2005, MNRAS, 357, 518
Kawahara, H. 2010, ApJ, 719, 1926
Kawahara, H., Kitayama, T., Sasaki, S., & Suto, Y. 2008, ApJ, 674, 11
LaRoque, S. J., Bonamente, M., Carlstrom, J. E., et al. 2006, ApJ, 652, 917
Lau, E. T., Nagai, D., Kravtsov, A. V., & Zentner, A. R. 2011, ApJ, 734, 93
Leccardi, A., & Molendi, S. 2008, A&A, 486, 359
Lin, W., & Ishak, M. 2017, Phys. Rev. D, 96, 083532
Martino, R., Mazzotta, P., Bourdin, H., et al. 2014, MNRAS, 443, 2342
Mason, B. S., Myers, S. T., & Readhead, A. C. S. 2001, ApJ, 555, L11
Mazzotta, P., Rasia, E., Moscardini, L., & Tormen, G. 2004, MNRAS, 354, 10
Meneghetti, M., Rasia, E., Vega, J., et al. 2014, ApJ, 797, 34
Molnar, S. M., Birkinshaw, M., & Mushotzky, R. F. 2002, ApJ, 570, 1
Morandi, A., Nagai, D., & Cui, W. 2013, MNRAS, 436, 1123
Nagai, D., & Lau, E. T. 2011, ApJ, 731, L10
Nagai, D., Kravtsov, A. V., & Vikhlinin, A. 2007, ApJ, 668, 1
Nevalainen, J., David, L., & Guainazzi, M. 2010, A&A, 523, A22